Journal of Fluids and Structures (1995) **9**, 149–174

A NUMERICAL SIMULATION OF STEADY FLOW IN A 2-D COLLAPSIBLE CHANNEL

X. Y. LUO AND T. J. PEDLEY
Department of Applied Mathematical Studies, The University of Leeds
Leeds LS2 9JT, U.K.

(Received 23 February 1994 and in revised form 11 November 1994)

We have studied steady flow in a 2-D channel with one plane rigid wall and with a segment of the other wall replaced by an elastic membrane. Numerical solutions of the full governing equations have been obtained for Reynolds number Re = 1–600. The numerical method was to solve the Navier–Stokes equations for given membrane shape by using the finite element scheme FIDAP, and use the membrane equation to iterate for the membrane shape. The control parameters are the downstream transmural pressure, P_d, the longitudinal tension, T, and the Reynolds Number, Re. For a given Re and P_d, where $P_d = p_{external} - p_{internal} > 0$, there exists a limit of T, say T_c, below which no converged solution was found. There is a somewhat higher value, T_b, such that for $T_c < T < T_b$, the membrane bulges out at its upstream end while the downstream part still remains collapsed. It is extremely difficult, however, to obtain converged solutions with our numerical scheme as we decrease the tension to T_b and below. To investigate whether the breakdown of the solution could be of physical origin, we analysed a simple 1-D model of the same flow, similar to that of Jensen & Pedley (1989). The results confirm that, for given Re and P_d, there is a value of T (T_b), below which the upstream part of the membrane bulges out, with collapse only in the downstream part. Similarly, for fixed T, there is a value of Re (Re_b) above which no fully collapsed solutions are attainable. The values of T_b at given Re and P_d agree very well with the numerical results, especially for higher Re. Further, a qualitative comparison of our analytical predictions with the experimental measurements in a collapsible tube by Bonis & Ribreau (1978), show that it is near the bulging points that steady flow gave way to self-excited oscillations.

1. INTRODUCTION

THE COLLAPSE OF COMPRESSED ELASTIC TUBES conveying a flow occurs naturally in several physiological applications, e.g. blood flow in arteries and veins, urine flow in the urethra and the flow of air in the lungs during a forced expiration (Shapiro 1977; Kamm & Pedley 1989). In laboratory experiments on a finite length of collapsible tube, mounted on rigid tubes and contained in a chamber whose pressure can be controlled, with flow driven through at realistic values of the Reynolds number (in the hundreds or above), self-excited oscillations invariably arise in particular regions of parameter space (Conrad 1969; Brower & Scholten 1975). The thorough experiments of Bertram, in particular, have revealed a rich variety of periodic and chaotic oscillation types, demonstrating that the system is a nonlinear dynamical system of great complexity (Bertram 1982; Bertram *et al.* 1990, 1991). However, despite the existence of a number of theoretical models, revealing several different oscillation mechanisms, there is as yet no complete theoretical description of the oscillations in any realizable experimental conditions.

Most previous models have been either one-dimensional, in which flow variables are integrated across a vessel cross-section and therefore depend only on the longitudinal coordinate $\bar{x}$ and time $\bar{t}$, or the even cruder lumped-parameter models in which they

0889–9746/95/020149 + 26 $08.00

are integrated along the vessel too and so depend only on $\bar{t}$. The standard 1-D models [e.g., Shapiro (1977)] led to the conclusion that steady flow cannot exist in a collapsible tube if the flow velocity is anywhere as large as the speed of propagation of small-amplitude pressure waves, so choking and unsteady motion must result. Early, local theories ignored the external, rigid parts of the flow system, so the unsteady motion that occurs after choking could not be described. The lumped models [e.g., Katz *et al.* (1969)] can describe the system as a whole, but exclude choking and are of limited value. In a more recent model of a finite-length tube, the 1-D equations for fluid flow and tube elasticity are coupled to the up- and downstream rigid segments. Moreover, the model incorporates important features of the real system, such as viscous energy loss in the intermittently separated flow downstream of the point of greatest collapse and longitudinal tension in the tube wall (Cancelli & Pedley 1985; Jensen & Pedley 1989). This model predicts nonexistence of a steady flow in some regions of parameter space and instability in others. Nonlinear analysis has enabled some features of the experimental observations to be qualitatively reproduced (Jensen 1990).

Even in the better models, however, some of the important dynamical factors are described extremely crudely, using *ad hoc* formulae that are incapable of systematic improvement. Two examples are: (a) taking the energy loss downstream of the constriction to be proportional to $-\partial\bar{u}^2/\partial\bar{x}$, where $\bar{u}$ is the cross-sectionally averaged longitudinal velocity and $\bar{x}$ the axial coordinate; and (b) stating that the transmural (external minus internal) pressure difference is equal to the sum of a tube law term (as if the tube were longitudinally uniform) and a longitudinal tension proportional to $\partial^2\bar{A}/\partial\bar{x}^2$, where $\bar{A}$ is the cross-sectional area (as if the tube wall were a 2-D membrane) (Cancelli & Pedley 1985). The latter is a poor representation of nonaxisymmetric, large deformation shell theory for a finite-length, end-supported cylinder, but to improve it requires a substantial computational effort. To improve the former also requires a big computational programme, in which the full Navier–Stokes equations are solved numerically for the appropriate geometry.

Because of the difficulty and large computational requirements for the full three dimensional solution of the above problems, we have embarked on a programme to provide a complete determination of steady and unsteady flow, including the self-excited oscillations, in a simpler, but in principle realizable, two-dimensional version of the same problem. The flow configuration is as depicted in Figure 1: part of one wall of a two-dimensional channel is replaced by an elastic segment, and steady flow is assumed upstream. The displacement of the segment is determined from the hydrodynamic stresses acting on it. In contrast with the usual models, the elasticity of this segment can be described rationally, by treating it as a membrane, with constant or variable tension, or as a beam with bending stiffness. Wall inertia, as well as fluid inertia, can be taken into account. Hitherto, a sequence of subproblems has been examined, building up towards the full time-dependent solution at high values of the Reynolds number, Re.

The first subproblem was based on steady lubrication theory, on the assumption that the wall slope remained small and that inertia was negligible (Pedley 1992). The membrane tension was either uniform or decreasing with distance downstream as a result of viscous shear stress. For a given channel, the solution was shown to depend on two dimensionless parameters involving the flow rate, $\bar{Q}$, the transmural pressure difference at the downstream end of the elastic segment ($\bar{P}_F = \bar{p}_e - \bar{p}_F$, see Figure 1) and the membrane tension at the downstream end, $\bar{T}_d$. One of the main results was the demonstration that at least one steady solution exists for all positive values of $\bar{Q}$, $\bar{P}_F$

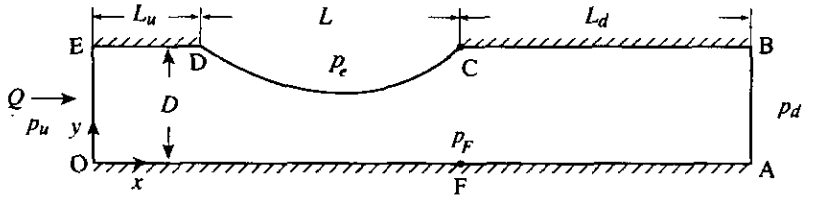

Figure 1. The geometry of the 2-D collapsible channel.

and $\bar{T}_d$. This analysis was not uniformly valid for all $\bar{T}_d$, because the wall slope became large at the downstream end when $\bar{T}_d$ was small. The second sub-problem was therefore to abandon the lubrication approximation, but still neglect inertia and solve the Stokes equations for the fluid flow and pressure fields. This has been done with the Finite Element Method (FEM) applied to the stream-function-vorticity equations (Lowe & Pedley 1994). Calculation of the membrane deformation has to be performed iteratively: guess the shape, compute the pressure (and wall shear stress) distributions, update the shape according to a finite-difference form of the geometrically nonlinear membrane equations, and so on. For given $\bar{Q}$ and $\bar{P}_F$, and sufficiently large $\bar{T}_d$ (assumed uniform), the results agree with those of lubrication theory. More recent computations (Lowe & Pedley 1995) have shown that for any set of $\bar{Q}$ and $\bar{P}_F$ values, a solution cannot be found for arbitrarily small $\bar{T}_d$. This appears to conflict with the lubrication theory results; we believe the cause to lie in the numerical procedure rather than the difference between the two models (Silliman & Scriven 1980) and further work is proceeding.

In this paper, we consider steady flow at nonzero Reynolds number with uniform tension in the membrane. The approach is to use a standard 2-D Navier–Stokes (N–S) solver for the flow field, and iterate for the wall position as outlined above. The flow solver used is FIDAP, an FEM package in primitive variables which is extremely reliable for 2-D laminar flows. It is again found that, for a given downstream transmural pressure and Re, a steady solution cannot be attained for sufficiently small tension.

This result also conflicts with that of the corresponding high-Reynolds-number 1-D model, a modification of that of Jensen & Pedley (1989), which has a solution for all $\bar{T}_d$. However, the numerical and model solutions agree in predicting that, as $\bar{T}_d$ is reduced, the membrane tends to bulge out near its upstream end, while remaining severely collapsed downstream (the same was found using lubrication theory). There is fair quantitative agreement between the models in the predicted values of $\bar{T}_d$ at which bulging first begins (for given $\bar{P}_d$ and $\bar{Q}$), especially at larger Reynolds numbers.

The problem is formulated in the next section, and the numerical method described in Section 3. Section 4 contains the numerical results, which are discussed with reference to the simple 1-D model (valid, if anywhere, for high Reynolds number) in Section 5. Further discussion and conclusions are presented in Section 6.

2. FORMULATION

Steady, incompressible flow of a Newtonian fluid in the channel depicted in Figure 1 is considered. The governing equations for the flow in the channel are expressed in a nondimensional form:

$$\mathrm{Re}\, u_j u_{i,j} = -p_{,i} + u_{i,jj}, \tag{1}$$

$$u_{i,i} = 0, \tag{2}$$

where $\mathrm{Re} = \bar{U}_0 \bar{D} \rho / \mu$ is the Reynolds number, $\bar{U}_0$ is the characteristic velocity, here taken to be the mean velocity at the entrance of the channel, $\bar{D}$ is the undistorted channel width, and μ, ρ are the fluid viscosity and density. The dimensionless variables are related to the physical variables (with overbar) in the following way:

$$u_i = \bar{u}_i / \bar{U}_0, \quad i = 1, 2; \quad p = \bar{p} \bar{D} / \mu \bar{U}_0; \quad x = \bar{x} / \bar{D}; \quad Y = \bar{y} / \bar{D}.$$

Boundary conditions on u_i are those of no slip at the side walls and a parabolic velocity profile at the entrance. Parallel outflow is assumed which implies $u_2 = 0$ and constant normal stress at the outflow boundary far downstream, i.e.

$$\begin{aligned} u_1(x, y) &= 6y(1 - y), \quad & u_2(x, y) &= 0 \text{ along OE;} \\ u_1(x, y) &= 0, & u_2(x, y) &= 0 \text{ along ED, DC, CB and OA;} \\ -p + 2\partial u_1(x, y)/\partial x &= p_d, & u_2 &= 0 \text{ along AB;} \end{aligned}$$

where p_d is a given constant.

The downstream boundary is for most calculations taken to be 7 channel widths downstream of the elastic segment ($L_d = 7$). For lower values of Re, this is long enough for the parallel boundary condition to be applicable for the outflow. We are aware that, for high Reynolds number, the downstream length may not be long enough for the flow to recover entirely from the disturbance caused by the collapsed wall. We have tested three different downstream lengths, $L_d = 4$, $L_d = 7$ and $L_d = 11$ at $\mathrm{Re} = 500$, and the wall vorticity distributions for these different downstream lengths show that $L_d = 7$ is long enough for this problem [see Figure 3(a) below].

The elastic segment of the upper wall DC is assumed to be a thin membrane, distorted by the difference between the internal and external pressure. It obeys the dimensionless equation

$$p_e - p = T/R, \tag{3}$$

where $T = \bar{T} / \mu \bar{U}_0$, $\bar{T}$ is the uniform tension in the membrane, and R is the dimensionless radius of curvature. If we express R in terms of the channel width $h(x)$, equation (3) becomes

$$p_e - p = Th''(1 + h'^2)^{-3/2}; \tag{4}$$

where a prime denotes differentiation with respect to x.

In this paper, we take Re (equivalent to dimensionless flowrate), T, and $P_d = p_e - p_d$ (where p_d was arbitrarily chosen as zero in the calculations) as control parameters. This last differs somewhat from the control pressure difference chosen by other workers (Brower & Scholten, 1975; Bertram 1986; Jensen & Pedley 1989; Lowe & Pedley 1994), who all used the transmural pressure difference at the downstream end of the collapsible segment ($P_F = p_e - p_F$) instead. Conrad (1969) used P_d as defined here.

The parameter values chosen here as follows:

$$\begin{aligned} &\mu = 1 \times 10^{-3} \text{ Pa s}, \quad & &\rho = 10^3 \text{ kg/m}^3, \quad & &\bar{D} = 10^{-2} \text{ m}, \\ &\bar{L} = 5 \times 10^{-2} \text{ m}, \quad & &\bar{L}_u = 2 \times 10^{-2} \text{ m}, \quad & &\bar{L}_d = 7 \times 10^{-2} \text{ m}, \\ &\bar{T}_0 = 1{\cdot}610245 \text{ N/m}, \quad & &\bar{P}_{d0} = \bar{p}_e - \bar{p}_d = 0{\cdot}93 \text{ Pa}. \end{aligned}$$

The suffix zero on $\bar{T}_0$ and $\bar{P}_{d0}$ indicates that these are reference values, chosen to permit direct comparison with Lowe and Pedley's (1994) results; a range of values for each parameter was used in the calculations, as indicated below. The nondimensional parameter values are: $L = 5$, $L_u = 2$, $L_d = 7$ (see Figure 1). The Reynolds number

Figure 2. The finite element mesh of the flow domain (mesh-3), with 1642 6-node triangular elements and 3261 nodes.

investigated is in the range of $\mathrm{Re} = 1 - 600$, (or $\bar{U}_0 = 1 - 600 \times 10^{-4}$ m/s). The nondimensionalization of $\bar{T}$ and $\bar{P}_d$ shows that the dimensionless T and P_d are not independent of Re; in fact $T_0 = T_0^*/\mathrm{Re}$, $P_{d0} = P_{d0}^*/\mathrm{Re}$, where $T_0^* = 1{\cdot}610245 \times 10^7$, $P_{d0}^* = 9{\cdot}3 \times 10^4$.

3. METHOD

We mainly use the finite element method in our numerical calculations. The major difficulty in the calculations is that the position of the elastic wall determined by equation (4) is governed by the transmural pressure, $p_e - p$, which is itself affected by the flow field in the channel, and that in turn is determined by the wall shape. In this paper, we use successive approximations to approach the final solution, i.e., we solve the flow problem and the wall equation separately, but exchange the boundary information in an iterative way. In the following section, the method is explained in detail.

3.1. The Flow Domain

We use the FIDAP Fluid Dynamic Package to perform the FEM calculations for the flow domain. The finite element grid is shown in Figure 2. A 6-node triangular element is used here since this type of element is flexible and fits well with any boundary positions that occur in the successive approximations of the wall shape. Velocities, u_i, and pressure, p, are approximated by their nodal values, U_i and P, through

$$u_i(x) = \phi^T U_i, \quad i = 1, 2, \tag{5}$$

$$p(X) = \psi^T P, \tag{6}$$

where X is the vector of nodal coordinates, and ϕ and ψ are the standard interpolation functions of the 6-node triangular element; their expressions can be found in any FEM textbook, [e.g., Zienkiewicz (1980)].

Substituting equations (5) and (6) into equations (1) and (2), and invoking the Galerkin residual method, we obtain the typical finite element matrix equation

$$K(V)V = F, \tag{7}$$

where

$$V = \begin{Bmatrix} U_1 \\ U_2 \\ P \end{Bmatrix} \tag{8}$$

are the column vectors of velocities and pressures at the element nodal points; K is the coefficient matrix composed of integrals of the interpolation functions; F is the general external force vector introduced by boundary conditions (FIDAP 1992a).

The matrix equation (7) is a set of nonlinear equations which need to be solved iteratively. A Quasi-Newton iteration method (Broyden-updated) is used here following a few fixed point iterations (FIDAP 1992b).

The convergence criteria for the kth iteration are

$$\|\Delta V_k\|/\|V_{k-1}\| < \text{VTOL}, \qquad \|R(V_k)\|/\|R_0\| < \text{RTOL}, \tag{9, 10}$$

where $R(V_k)$ is the residual vector of equation (7) at the kth iteration, and R_0 is the initial residual vector, $R_0 = R(V_0)$; $\|.\|$ is the Euclidean norm, and VTOL and RTOL are the tolerance values. In this study, we choose VTOL = RTOL = 0·01 and found the accuracy of the flow solution to be satisfactory. We tested smaller values of VTOL and RTOL, which needed a few more iterations but still gave convergence to a solution which was graphically indistinguishable everywhere (except for the singular vorticity at the upstream corner $x = 2$, $y = 1$ in cases where the membrane bulged out—see below).

3.2. The Elastic Wall

To solve the membrane equation (4) numerically, we discretize the elastic segment L into n line elements with $n + 1$ nodes. In this part of the calculation we take the number of the nodes and the position of each node to be identical to those in the boundary DC of the flow domain, so that subsequently information can be readily exchanged on this boundary. For this reason, the nodes here are in general not equally spaced in x. Let

$$\delta_i = x_i - x_{i-1}, \qquad \delta_{i+1} = x_{i+1} - x_i;$$

by using a central finite difference scheme for equation (4), we have

$$\frac{\delta_{i+1}}{\delta_i + \delta_{i+1}} h_{i+1} - h_i + \frac{\delta_i}{\delta_i + \delta_{i+1}} h_{i+1} + \frac{\delta_i \delta_{i+1}}{2} \frac{P_e - P_i}{T} \left[1 + \left(\frac{h_{i+1} - h_{i-1}}{\delta_i + \delta_{i+1}}\right)^2\right]^{3/2} = 0, \tag{11}$$

or, in matrix form,

$$R(P, H) = 0, \tag{12}$$

where H is a column vector of the nodal values of h_i, P is the pressure imposed by the fluid upon the boundary. The Newton–Raphson method is used to solve nonlinear equation (12). The convergence criterion for the jth iteration is to demand that the residual vector $R_j = R(P, H^j)$, satisfy

$$\|R_j\| < \varepsilon,$$

where ε is chosen to be in the range of 10^{-4}–10^{-6} in the iteration. We have checked that the difference in wall shape between $\varepsilon = 10^{-4}$ and $\varepsilon = 10^{-6}$ is imperceptible, but we nevertheless used $\varepsilon = 10^{-6}$ in almost all computations ($\varepsilon = 10^{-4}$ was occasionally used when convergence of the wall shape solution was very slow).

3.3. The Coupled Solutions for the Flow and The Elastic Wall

Having obtained the numerical schemes for the flow equations and the wall equation, we now try to find the solution which satisfies the two sets of equations simultaneously. The successive approximation scheme can be summarized as follows.

(a) Choose an initial wall shape and start the whole iteration. If we use k as the iteration number, then for $k = 0$, we choose

$$H^{(0)} = H^{\text{initial}}.$$

(b) At the kth iteration, generate a finite element mesh according to the given wall shape $H^{(k)}$ by using the FIDAP mesh generator FIMESH.

(c) Start a sub-iteration and using the FIDAP solver to solve the nonlinear matrix equation, equation (7), in the flow domain with boundary $H^{(k)}$. The result is that the updated pressure and velocity vector, $V^{(k)}$, are obtained from

$$K(V^{(k)})V^{(k)} = F.$$

(d) Take the pressure, $P_i^{(k)}$, $i = 1, \ldots, n+1$, along the boundary DC from the above solution, $V^{(k)}$, and use it to replace P_i in equation (11). We can then start a sub-iteration to solve the nonlinear membrane equation (12). As a result, the wall shape now is updated to $H^{(k+1)}$, where

$$R(P^k, H^{k+1}) = 0.$$

(e) Compare the new wall shape, $H^{(k+1)}$, with the previous one, $H^{(k)}$, to check if they satisfy the following criterion:

$$|H^{(k+1)} - H^{(k)}| \leq \varepsilon_1,$$

where ε_1 is a tolerance parameter, taken to be 10^{-6}. If the convergence criterion is satisfied, then the solution, $V^{(k)}$, we obtained for the flow and pressure fields and the wall shape, $H^{(k+1)}$, constitute the coupled solution satisfying both the flow and the elastic wall equations. In most of the converged cases, convergence was achieved in fewer than 100 iterations.

Divergence of the whole iteration can occur, especially when the longitudinal tension T is small. As T is reduced, the other parameters remaining fixed, the solution first becomes sensitive to small changes of wall shape during sub-iteration (c). Next, the curved wall shape appears to "oscillate" between iterations, taking one shape for k even and another for k odd; in some cases, when the deformation is large, this oscillation can cause the membrane to appear to intersect the opposite wall. In all such cases, we deem the numerical steady-state model to have broken down; such breakdown typically occurred after only about 20–30 iterations.

The question we need to ask is whether this failure of convergence is caused by an intrinsic property of the original physical system or is simply due to the use of an inadequate numerical procedure. To investigate the first possibility, we have analysed a simple one-dimensional model simulating the same problem and this will be discussed in Section 5.

To minimize the latter possibility, we have conducted four separate tests for accuracy and convergence, as follows.

(i) *Choice of the element mesh*

A typical element mesh is shown in Figure 2. The mesh was denser near the compliant wall, especially in the region of the joints with the rigid walls, where sharp changes in velocities and pressure are expected. We do not change the number of elements during the iterations, to avoid additional complexity, but we do adjust the position of each node for every updated wall boundary to keep the smoothness of the grid.

The number of elements and the allocation of nodes were decided after a series of mesh refinements undertaken to achieve the required accuracy. We have tested four

different mesh designs: mesh-1 (with 451 elements and 891 nodes), mesh-2 (with 1044 elements and 2065 nodes), mesh-3 (1642 elements and 3261 nodes), and mesh-4 (2134 elements and 4465 nodes). Other studies [e.g., Ralph & Pedley (1988), Tutty & Pedley (1993)] have shown that the computed vorticity at the wall is the most sensitive indicator of numerical inaccuracy, especially near sharp corners. Therefore, the vorticity distribution along the wall containing the membrane was compared for the four meshes at $\mathrm{Re} = 500$ and the same T and P_d. Figure 3(b) shows that numerical pressure and vorticity oscillations exist for mesh-1 since it is too coarse, but the solution curve starts to look stable for mesh-2 and only slight differences are observed between mesh-2 and mesh-3, while the solution of mesh-3 is very close to (most of it is

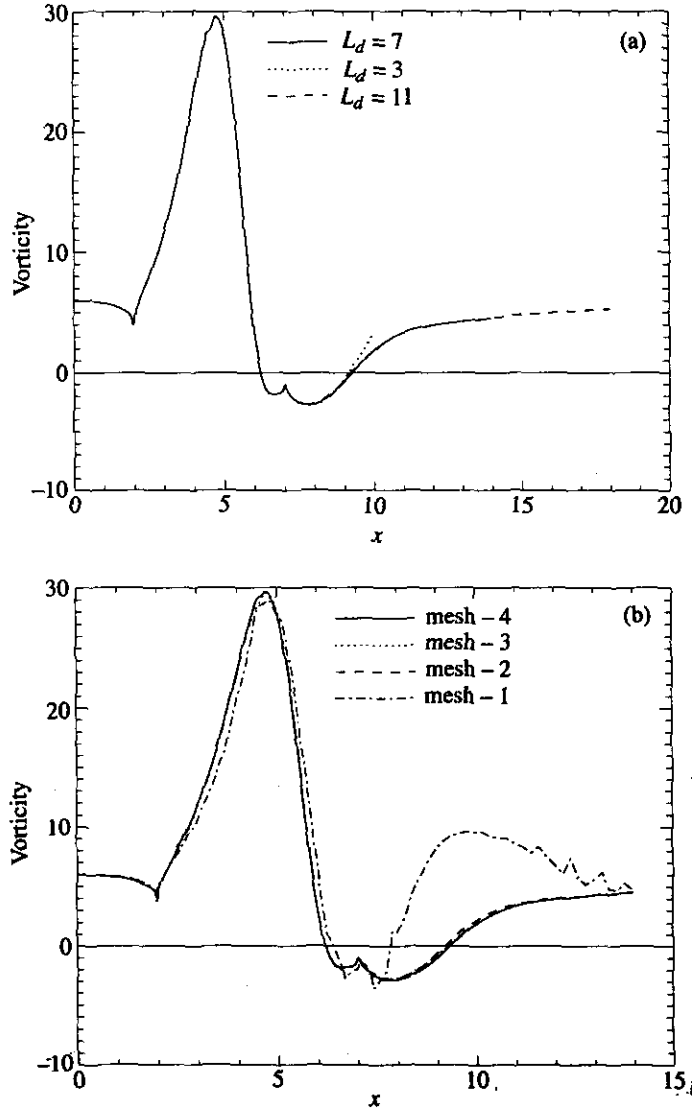

Figure 3. (a) The wall vorticity distribution for flow at $\mathrm{Re} = 500$, $T^* = T_0^*/16{\cdot}5$, $P_d^* = P_{d0}^*$, with downstream length, $L_d = 3$, 7, 11, respectively. (b) The wall vorticity distribution for flow at the same parameter values as above with the mesh chosen as mesh-1, mesh-2, mesh-3, and mesh-4, respectively. Note that the elastic membrane occupies the region $2 \leq x \leq 7$.

graphically indistinguishable from) that of mesh-4. Therefore mesh-3 (Figure 2) is chosen in our computation.

(ii) *Use of a relaxation method to update the wall shape*

To avoid the "oscillation" of the wall shape referred to above, we update the wall shape not only using its current iterative value, but also its previous value:

$$H^{*(k+1)} = (1-\alpha)H^{(k+1)} + \alpha H^{(k)}. \tag{13}$$

Here, the relaxation parameter, α, is chosen in the range of 0·5–0·9; 0·9 was chosen for the smallest value of tension. The intermediate value, $H^{*(k+1)}$, is used as the next wall position in step (b). Such relaxation enabled us to obtain a solution for smaller values of T than without it, but even with α as large as 0·9, a converged solution was in many cases unattainable if T was too small.

(iii) *Approaching the minimum tension decrementally*

The choice of initial wall shape and the flow field can be very important in obtaining a converged final solution. For larger tension, we can use a straight line as the initial wall shape and zero initial flow and approach the final solution without any problem. But this initial guess would fail to give convergence when the tension was small. To achieve lower tensions, therefore, we start from a large T and decrease it gradually, using the converged solution for $T = T_1$ (say) as the initial guess for $T = T_1 - \delta T$. Thus, the initial wall shape and the flow are adjusted decrementally and this helps us to bring the tension to a lower value.

(iv) *Comparison with the solution obtained by a different numerical method*

For very small values of Re, the solutions have been compared with those obtained by Lowe & Pedley (1994) at Re = 0. They wrote a different FEM code which uses the stream-function and vorticity as dependent variables, and solved the Stokes equation and the membrane equation for parameter values that are otherwise the same as those used here. We obtained virtually identical wall shapes for all the five different parameter groups used by them:

$$P_F = -991{\cdot}53, \quad T = 211546{\cdot}6; \qquad P_F = 1689, \quad T = 535{\cdot}5;$$
$$P_F = 905{\cdot}32, \quad T = 161024{\cdot}5; \qquad P_F = 184{\cdot}28, \quad T = 86909{\cdot}7;$$
$$P_F = 48{\cdot}05, \quad T = 1540{\cdot}6.$$

These values were chosen to correspond with the earlier lubrication theory analysis by Pedley (1992), who used a different nondimensionalization. Note that they fixed pressure at point F, while we fixed pressure at the downstream end AB. The pressure drop from point F to A was estimated by assuming a Poiseuille flow for the rigid part since only low Re flow was considered. It was also found that Re = 0 and Re = 1 gave virtually the same wall shape for these parameter values.

In a more recent work (Lowe & Pedley 1995), these authors have failed to find a

converged solution, even at Re = 0, if the tension is taken to be too small. This holds both for uniform T, as here, and for a case in which T varies along the channel as a result of viscous shear stress. On the other hand, Pedley (1992), using the approximation of lubrication theory, demonstrated the existence of a solution for all positive T. It is thus still not certain whether our finding, that at higher Reynolds numbers there seems to exist a value of the tension below which no steady solution can be obtained, is of physical or numerical origin. To investigate this problem, we develop a simple but *ad hoc* one dimensional model of the same flow in Section 5.

4. RESULTS

Before we present the results and discuss how they vary with the control parameters Re, T and P_d, we note that our nondimensional scaling means that T and P_d depend on the mean velocity, $\bar{U}_0$ (see Section 2). In order to avoid confusion and permit easier comparison with experiments, in which flow rate is varied with $\bar{P}_d$ and $\bar{T}$ held constant, we shall use the parameters T^* and P^*_{d0} in discussing our results, where $T = T^*/\mathrm{Re}$, $P_d = P^*_{d0}/\mathrm{Re}$ (see Section 2). Accordingly, the calculated pressure, p, will be transformed into $p^*(p = p^*/\mathrm{Re})$ in the results.

For $P^*_d = P^*_{d0}$, and Re in the range of 1–500, we obtained a group of solutions for different values of T^*, where T^* is decreased from T^*_0 by a factor of β, $(T^* = T^*_0/\beta$, $\beta \geq 1)$. The corresponding wall shape, the pressure drop distribution and the wall vorticity distribution along the upper, elastic wall are shown in Figures 4–6(a,b,c) for Re = 1, 100, and 500.

Figures 4–6 show that the wall deflection at first increases as the tension is reduced. For Re = 1 (Figure 4), the reduction continues until a critical value of T^* is reached (T^*_c), below which no converged solution occurs.

However, for Re = 100 and 500 (Figures 5 and 6), the maximum deflection of the membrane reaches a limit at a certain value of T^*; as T^* is reduced further, the membrane slope at the downstream end continues to increase, but the maximum deflection does not. At a particular value of T^*, e.g. T^*_b, the membrane slope becomes zero at the upstream end ($\beta_b = T^*_0/T^*_b \simeq 101$ for Re = 100, $\beta_b \simeq 21$ for Re = 500), and for lower T^* the upstream part of the membrane bulges out. Shortly thereafter, the critical value, T^*_c, is reached and no further solution can be obtained.

As T^* is reduced, the pressure drop and the maximum wall vorticity increase. No flow separation is found for Re = 1, whatever the value of T^*, or for high Re and large T^*. For larger Re, however, reducing the tension causes the flow to separate, as evidenced by the negative wall vorticity (shear stress). Separation is a consequence of the pressure rise downstream of the constriction. Note that the point of minimum area (and pressure) moves downstream as T^* is reduced, while the separation point at first moves upstream and then downstream again.

As Re rises, the shapes of the plotted curves change. Figure 7(a,b,c) shows the results when we increase Re while fixing the tension at $T^* = T^*_0/20$. The point of greatest constriction tends to move downstream more, and the upstream half of the channel opens up more than the downstream half as Re becomes larger. An upstream bulging and downstream movement of the constriction as flowrate is increased was also found by Jensen & Pedley (1989) using a one-dimensional model. We also find, as they did, that the degree of constriction does not necessarily continue to increase as Re rises. In fact, for a certain value of Re, the degree of constriction reaches a maximum, and then starts to decrease even before the upstream membrane bulges out; see Figure 12(b) later for details. As Re rises to 600, we failed to obtain a converged solution even after

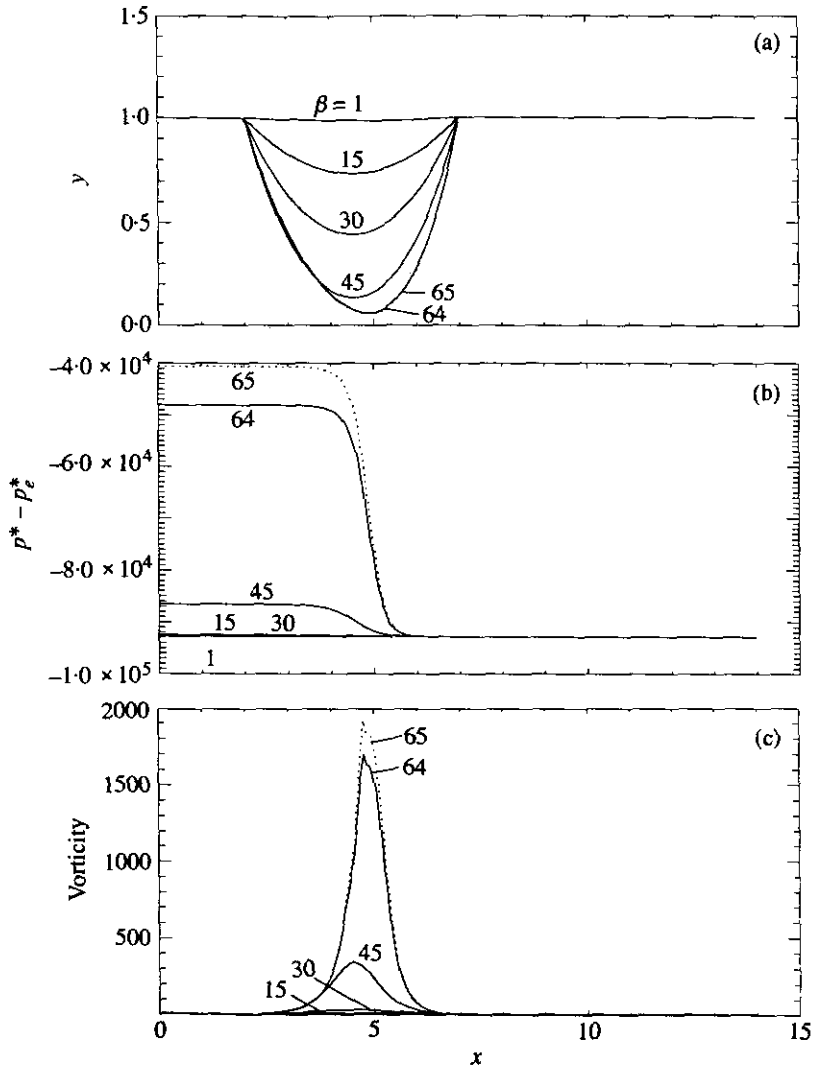

Figure 4. (a) The wall shape, (b) the pressure distribution, and (c) the wall vorticity distribution, obtained from the numerical calculations at Re = 1 and $P_d^* = P_{d0}^*$, and $T^* = T_0^*/\beta$ ($\beta = 1$, 15, 30, 45, 64). No solution was found at $\beta = 65$ or below (the dotted curves show the last iteration for $\beta = 65$ before the calculation was stopped).

200 iterations; in any case, the solution woiuld be inaccurate then because the effect of the downstream boundary condition would be felt at the membrane.

On the other hand, not only does the shape vary, the magnitude of the pressure drop and the peak vorticity also increase significantly with Re. From the vorticity distribution in Figures 5–7, we can see how the flow separation region (indicated by the two points at which wall vorticity changes sign) changes with T^* for fixed Re, and with Re for fixed tension. It seems that increasing Re or decreasing tension have similar effects on this.

The region of reversed flow extends downstream for some distance along the rigid wall. Figure 8 shows the streamlines of the whole flow field at $T^* = T_0^*/107$, Re = 100 and $P_d = P_{d0}^*$, showing the flow separation more clearly.

Figure 9(a,b) shows how, when the tension is fixed ($\beta = 20$, 30 and 40), the overall

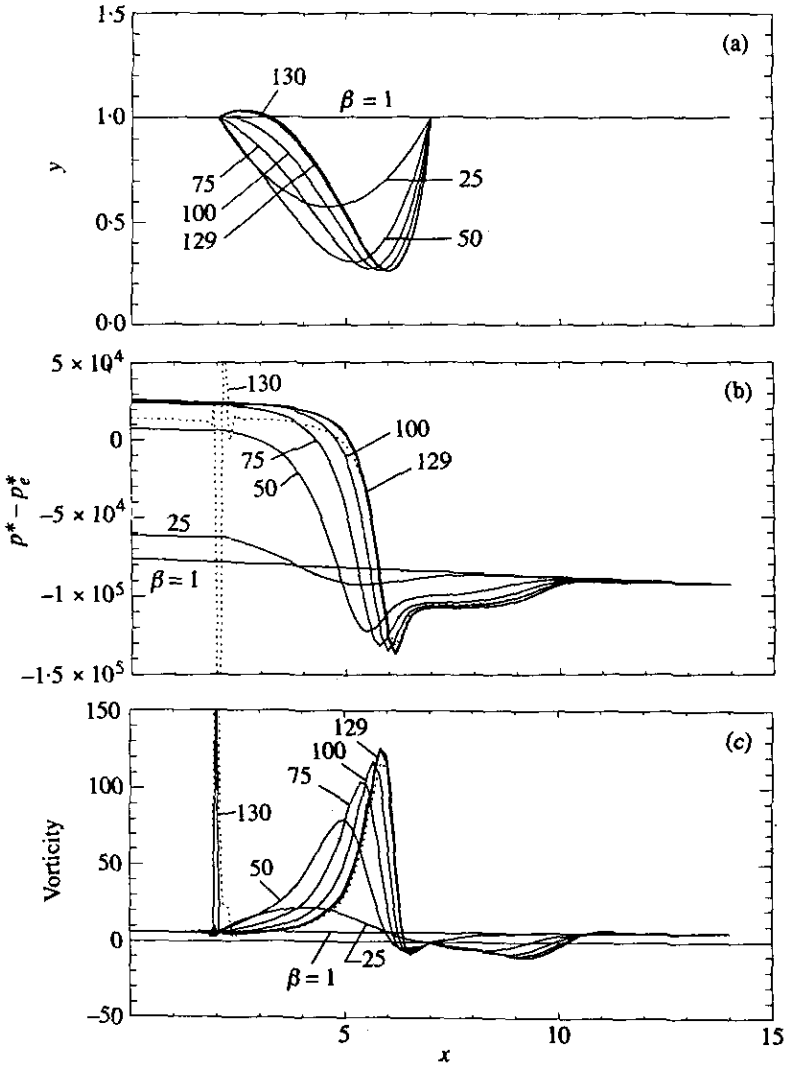

Figure 5. (a) The wall shape, (b) the pressure distribution, and (c) the wall vorticity distribution, obtained from the numerical calculations of Re = 100 and $P_d^* = P_{d0}^*$, and $T^* = T_0^*/\beta$ ($\beta = 1$, 25, 50, 75, 100, 129). The iteration that diverged is marked by dotted curve for $\beta = 130$.

pressure drop along the channel and the minimum value of the channel cross-section area, A, ($= h_{min}$) change with increasing Re. The points marked with stars on the computed curves (dashed lines) represent the value of Re (Re_b) at which the upstream bulge first appears. The curves come to an end at the somewhat larger Re (Re_c) beyond which no solution could be found. The other curves are the prediction of the simple model of Section 5, and will be discussed later.

To find out how the downstream transmural pressure affects the solution, we also calculated solutions for two different values of P_d^*: $P_d^* = P_{d0}^*/2$, and $P_d^* = 2P_{d0}^*$. For more positive $P_d^* (= 2P_{d0}^*)$, the results look similar to those with lower tension; i.e., more deflection and larger slope of the $\Delta p^* = p_u^* - p_d^*$ versus Re curve. When the pressure inside the channel becomes more negative, the degree of collapse of the elastic membrane tends to be more severe, and the convergence of the solution fails at a lower value of Re.

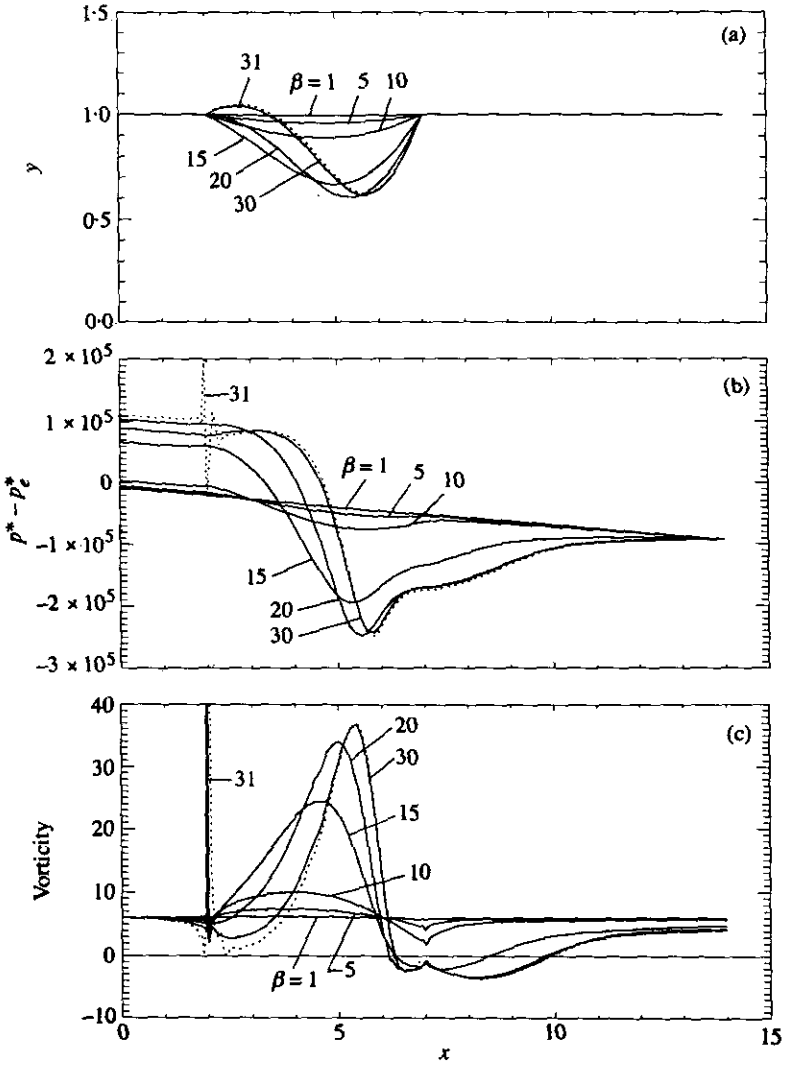

Figure 6. (a) The wall shape, (b) the pressure drop distribution, and (c) the wall vorticity distribution, obtained from the numerical calculations of Re = 500 and $P_d^* = P_{d0}^*$, and $T^* = T_0^*/\beta$, (β = 1, 5, 10, 15, 20, 30). The iteration that diverged is marked by dotted curve for $\beta = 31$.

However, when the downstream pressure is less positive, $P_d^* = P_{d0}^*/2$, we find that when Re increases above about 340, the upstream transmural pressure, $p_e - p_u$, becomes negative and a bulge begins; in this case, however, the whole elastic segment is eventually dilated [see Figure 10(a,b,c)], which should be compared with Figure 7(a,b,c). For this case, the numerical solution fails to converge at about Re = 560. The converged solution for Re = 540 is clearly inaccurate at the corners where the vorticity should be infinite [Figure 10(c)].

In obtaining these results we found that there is always a value of tension for each Reynolds number (except for Re = 1), T_0^*, at which the upstream membrane starts to bulge out. There is a corner at each end of the elastic membrane where it joins the rigid wall; until the upstream bulge appears, both corners are stagnation points in the sense that even an inviscid fluid would have zero velocity there. As a consequence, there is a (small) local rise in pressure, and a sharp fall in the magnitude of the wall vorticity. It

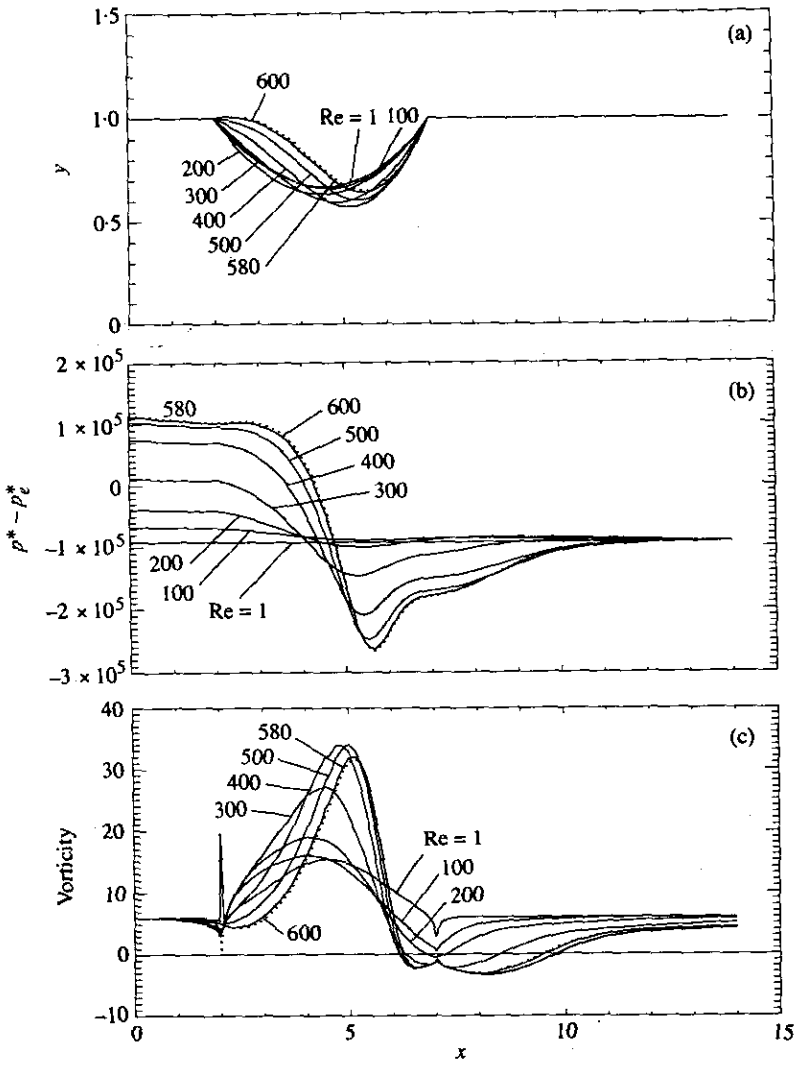

Figure 7. (a) The wall shape, (b) the pressure drop distribution, and (c) the wall vorticity distribution, obtained from the numerical calculations at $T^* = T_0^*/20$, $P_d^* = P_{d0}^*$, while Re = 1, 100, 200, 300, 400, 500, 580. The iteration limit was reached for Re = 600 (final iteration is marked by dotted curve) before convergence was achieved.

can be shown analytically that the vorticity at the corner point is zero (Moffatt 1964), but the numerical method does not resolve the very small length-scale over which that is achieved. When there is an upstream bulge, the upstream corner is convex to the flow. It follows that there must be a singularity in both the vorticity and the pressure at the corner (Moffatt 1964), and hence also in the membrane curvature. The singularity in the vorticity at Re = 100 and 500 is responsible for the spike in Figures 5(c) and 6(c),

Figure 8. The streamline contours of the flow at Re = 100, $T^* = T_0^*/107$, $P_d^* = P_{d0}^*$. A flow separation is developed downstream. Contour interval is 0·075.

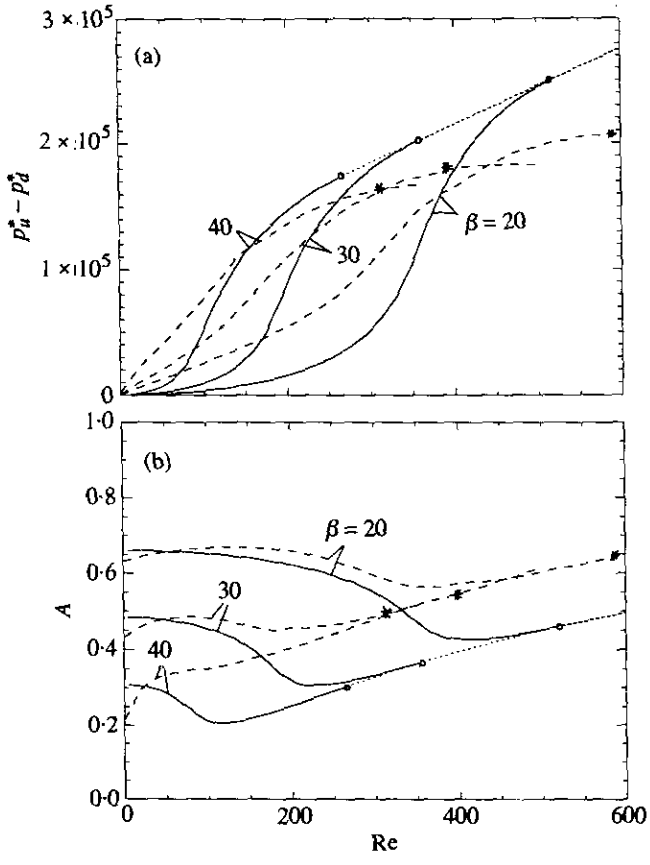

Figure 9. (a) The change of the pressure drop, $p_u^* - p_d^*$, with the increasing Re for $P_d^* = P_{d0}^*$, and three different values of tension $T^* = T_0^*/\beta$ ($\beta = 20$, 30, 40). Dashed curves are the numerical results, and the point where bulge-out first appears is marked by a star. The predictions from the analytical model in Section 5 are plotted as solid curves, with the bulging region indicated by dotted curves, and the first bulging point is marked by a circle. (b) The minimum wall deflection, A, versus Re at the same parameter values.

and inevitably has an influence on the flow and pressure at some distance from the corner (Ingham *et al.* 1990). The pressure singularity appears later than the vorticity, due to the smoothing effect of the finite resolution at the corner. However, when the bulge becomes more severe, a corresponding spike in the pressure occurs, as shown by the dotted curves in Figures 5(b)–6(b), representing an iteration in a sequence which fails to converge. To pursue a further numerical investigation for the bulged out case, the flow will probably need to be matched carefully to the analytical solution at the corner [see Bramley & Dennis (1984)].

5. AN ANALYTICAL MODEL

A steady one-dimensional model corresponding to our 2-D channel flow, incorporating a description of flow separation, is described in this section. The model is essentially the same as the earlier model of Jensen & Pedley (1989), the differences being the absence of a tube law contribution to the pressure-displacement relation, and a different nondimensionalization (we use the same scaling as employed in the foregoing).

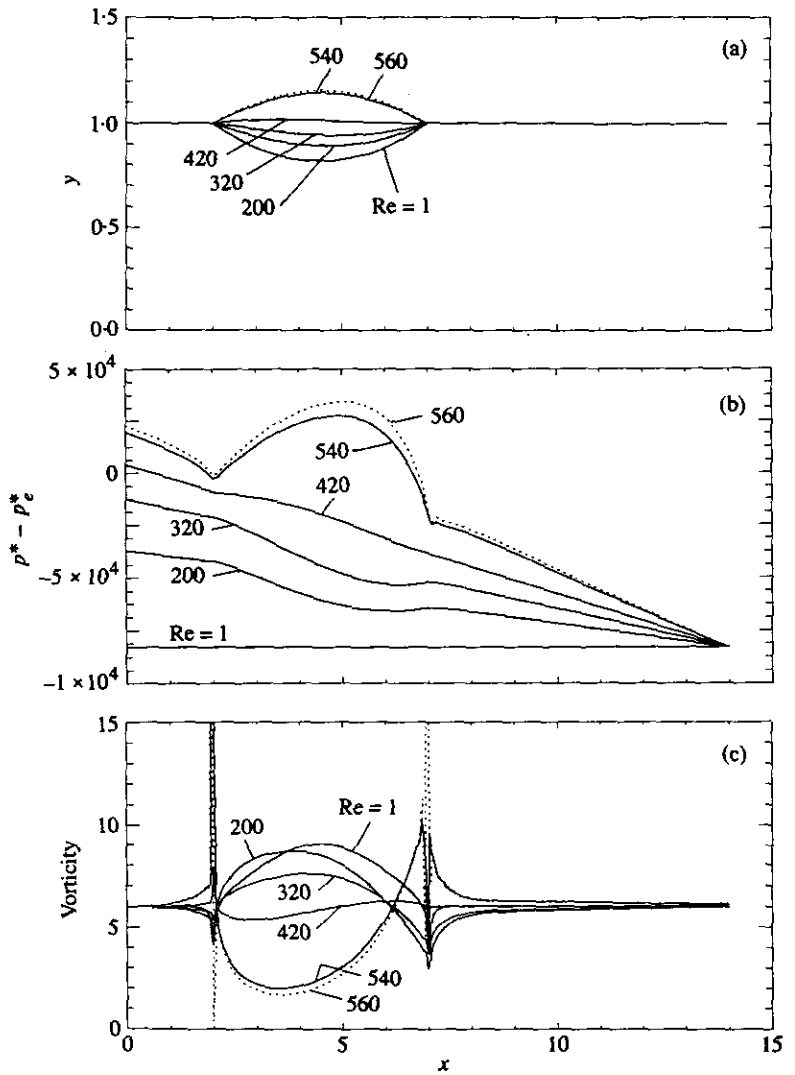

Figure 10. (a) The wall shape, (b) the pressure drop distribution, and (c) the wall vorticity distribution obtained from the numerical calculations at $T^* = T_0^*/20$, $P_d^* = P_{d0}^*/2$, and Re = 1, 200, 320, 420, 540. The wall shape bulges out when Re is larger than 320. Solution fails to converge for Re = 560 or higher (final iteration is marked by dotted curve).

5.1. Governing Equations

The unknown dimensionless variables are the channel width, $h(x)$, the longitudinal velocity, $u(x)$, and the pressure, $p(x)$. The governing equations are

Mass conservation

$$(uh)_x = 0. \tag{14}$$

Momentum

$$\mathrm{Re}\, uu_x = -p_x \qquad 0 \le x \le X_0, \tag{15}$$

$$\chi\, \mathrm{Re}\, uu_x = -p_x \qquad X_0 \le x \le \lambda. \tag{16}$$

Here $0<\chi<1$ is a constant, accounting for the energy loss downstream of a constriction when flow separation occurs, and X_0 is the (unknown) separation point [see also Cancelli & Pedley (1985)]. Note that this model does not include any energy loss upstream of the narrowest point, even in cases where the channel is dilated for part or all of its length so the flow separation might be expected at the upstream end. We consider only cases with constrictions for at least part of the length.

The membrane equation

$$p_e - p = h_{xx}; \tag{17}$$

note here that the radius of curvature is simplified to $1/R = h_{xx}$, because the 1-D model requires small membrane slope.

All the other dimensionless variables are chosen to be the same as those in Section 2, but instead of using diameter, the x coordinate is scaled according to the length scale

$$x = \bar{x}/\tilde{L}, \tag{18}$$

where the length scale, $\tilde{L}$, for longitudinal variation is chosen as

$$\tilde{L} = \left(\frac{\bar{D}^2\bar{T}}{\mu\bar{U}_0}\right)^{1/2} = \bar{D}\sqrt{T}. \tag{19}$$

The reason for choosing this length scale is to keep the equations (14)–(17) in a simple form: the longitudinal tension, T, does not explicitly appear in them. The influence of tension is seen only through the dimensionless length, λ,

$$\lambda = \bar{L}/\tilde{L} = L/\sqrt{T}. \tag{20}$$

The boundary conditions to the foregoing equations are

$$h(0) = h(\lambda) = 1, \tag{21}$$

$$p_u = p_e - h_{xx}(0), \qquad p_d = p_e - h_{xx}(\lambda). \tag{22, 23}$$

5.2. Solution and Results

Integration of equations (14)–(17) gives

$$h_{xx} = \begin{cases} P_u + \frac{1}{2}\,\mathrm{Re}(h^{-2} - 1), & 0 \le x \le X_0, \\ P_d + \frac{1}{2}\chi\,\mathrm{Re}(h^{-2} - 1), & X_0 \le x \le \lambda, \end{cases} \tag{24}$$

where P_u and P_d are defined as

$$P_u = p_e - p_u, \qquad P_d = p_e - p_d, \tag{25, 26}$$

respectively. P_d can be specified independently in advance, whereas P_u cannot. We assume that at the separation point, X_0, the wall reaches its lowest point, $h = A$

[following the notation of Jensen & Pedley (1989)], where $A \leq 1$. Then, from equation (24), we have

$$P_u = P_d - \tfrac{1}{2}(1-\chi)\,\mathrm{Re}(A^{-2}-1), \tag{27}$$

and the pressure drop along the elastic segment

$$\Delta p = p_u - p_d = \tfrac{1}{2}(1-\chi)\,\mathrm{Re}(A^{-2}-1). \tag{28}$$

Equation (28) shows that the pressure drop, Δp, along the compliant channel is affected by two factors: one is the geometric constriction represented by A here; if $A = 1$, i.e. the channel is straight, then $\Delta p = 0$. The other is the energy loss due to flow separation which is indicated by $(1-\chi)$; when $\chi = 1$, there is no energy loss, and when $\chi = 0$, there is no pressure recovery downstream, that is to say, all the dynamic pressure that is converted to kinetic energy in the parallel-sided jet downstream of the constriction is ultimately dissipated, by turbulence. Note that the only dissipation allowed for in the model is that due to flow separation; there is no direct viscous stress on the channel wall. The present model is therefore relevant only to high Reynolds number flow, and only to cases where the channel does experience a constriction.

Strictly speaking, χ should depend on A, but here we choose $\chi =$ constant for simplicity; Jensen & Pedley (1989) showed that the qualitative behaviour is unaffected by the value of χ, and we arbitrarily choose $\chi = 0{\cdot}5$. In order to calculate the pressure drop, equation (28), then, all we need is to find A, the degree of constriction. To determine A, we integrate equation (24) with respect to x:

$$h_x^2 = \begin{cases} -g_1(h) + \text{constant}, & 0 \leq x \leq X_0, \\ -g_2(h) + \text{constant}, & X_0 \leq x \leq \lambda, \end{cases} \tag{29}$$

where

$$\begin{aligned} g_1(h) &= 2P_u(1-h) + \mathrm{Re}(h^{-1}+h-2), \qquad 0 \leq x \leq X_0, \\ g_2(h) &= 2P_d(1-h) + \chi\,\mathrm{Re}(h^{-1}+h-2), \qquad X_0 \leq x \leq \lambda. \end{aligned} \tag{30}$$

At $h = A$, $h_x = 0$, so

$$h_x^2 = \begin{cases} g_1(A) - g_1(h) & 0 \leq x \leq X_0 \\ g_2(A) - g_2(h) & X_0 \leq x \leq \lambda. \end{cases} \tag{31}$$

Each of these equations can be integrated, giving relationships between A and the length of the relevant segment. Adding the two integrals together, we have a relationship between λ and A

$$\lambda = \int_A^1 \{[g_1(A) - g_1(h)]^{-1/2} + [g_2(A) - g_2(h)]^{-1/2}\}\,dh. \tag{32}$$

Thus, for given g_1, g_2, and λ, we can in principle determine A from the above integral. Once A is decided, we can easily calculate P_u and Δp from (27) and (28), respectively.

Equation (20) shows that (32) can be regarded as a relationship between the dimensionless tension T and A. It should be remembered that T involves the flow rate, through $\bar{U}_0$ [see equation (19)]. The problem now is to find out if there exists a limit of tension at given Re and P_d, below which no solution to the steady problem can be

found. To investigate this, we will examine the trajectories in the (h, h_x)-phase plane of the solutions of equation (24), as did Jensen and Pedley (1989). Let

$$X = h, \qquad Y = h_x;$$

then, using (28), we have

$$\begin{aligned} \dot{X} &= Y \\ \dot{Y} &= \tfrac{1}{2}\,\mathrm{Re}\,X^{-2} + (P_d - \tfrac{1}{2}\chi\,\mathrm{Re}) - \tfrac{1}{2}(1-\chi)\,\mathrm{Re}\,A^{-2}, \qquad 0 \le x \le X_0, \\ \dot{Y} &= \tfrac{1}{2}\chi\,\mathrm{Re}\,X^{-2} + (P_d - \tfrac{1}{2}\chi\,\mathrm{Re}), \qquad X_0 \le x \le \lambda, \end{aligned} \tag{33}$$

where a dot means d/dx. The equations for the phase plane trajectories obey different equations for the upstream part of the channel (lower half phase plane) and for the downstream part (upper half); examples are shown in Figure 11(a). The singular points

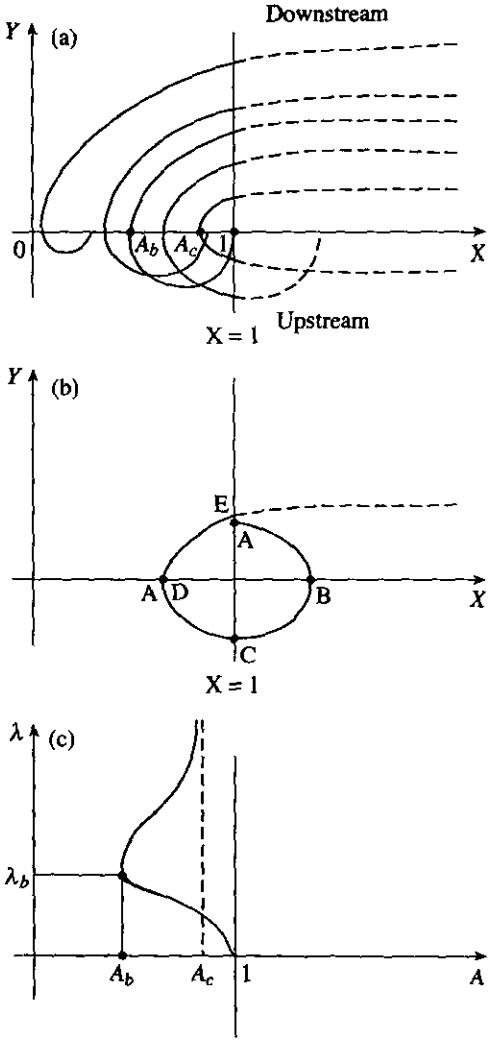

Figure 11. (a) The trajectories in the (h, h_x) phase plane ($X \equiv h$ and $Y \equiv h_x$). Since the channel is held open at both ends, the solution must cross $X = 1$ twice, with $h_x < 0$ and $h_x > 0$. (b) For $A_b \le A < A_c$, there are two values of λ, corresponding to a fully constricted solution (CDE), and a partially constricted one with upstream part bulged out (ABCD). (c) λ versus A.

occur when $Y = \dot{Y} = 0$; thus for the downstream part, there is a centre point at X_d, where

$$X_d = \sqrt{\frac{\chi \,\mathrm{Re}}{-(2P_d - \chi \,\mathrm{Re})}}, \tag{34}$$

and for the upstream part, the centre is at X_u, where

$$X_u = \sqrt{\frac{\mathrm{Re}}{-(2P_d - \chi \,\mathrm{Re}) + (1-\chi)\,\mathrm{Re}\,A^{-2}}}. \tag{35}$$

Now consider only the collapsed case when $2P_d - \chi \,\mathrm{Re} > 0$, so there is no real X_d, which means the downstream trajectories intersect the X-axis only once, at A. The upstream centre point, X_u, is a function of A, and it too has real values only when $A \le A_c$, where $A_c^2 = (1-\chi)\,\mathrm{Re}/(2P_d - \chi \,\mathrm{Re})$. For $A_c < A \le 1$ the upstream trajectories intersect the X-axis only once, like the downstream trajectories. As A decreases from A_c, however, the trajectories bend closer and closer to the X-axis. Eventually, the trajectories degenerate into a point at $X = 0$ as $A \to 0$ and $X_u \to 0$; see Figure 11(a).

The solutions which satisfy boundary condition (21) are those trajectories which intersect the line $X = 1$ both upstream and downstream (at $x = 0$ and $x = \lambda$). From Figure 11(a), we can see that such a solution does not exist when A is too small because then the upstream trajectory does not intersect the line $X = 1$. The minimum value of A, e.g. A_b, occurs just when the upstream trajectory intersects the X-axis at the two points $X = A_b$ and $X = 1$. Therefore, the condition to determine A_b becomes: there is a trajectory with $Y = 0$ at $X = 1$ and $X = A_b$.

From equation (31), the required condition is equivalent to

$$g_1(A_b) - g_1(1) = 0, \tag{36}$$

or

$$A_b = \frac{2(1-\chi)}{1 + \sqrt{1 + 4(1-\chi)(2P_d/\mathrm{Re} - \chi)}}. \tag{37}$$

For $\chi = 0{\cdot}5$, this has a simpler form, namely

$$A_b = \frac{1}{1 + 2\sqrt{P_d/\mathrm{Re}}}. \tag{38}$$

Relation (37) is valid only when $2P_d - \chi \,\mathrm{Re} > 0$, but that is in any case the condition for the channel to be collapsed ($X < 1$) towards the downstream end.

The above discussion shows that a steady solution exists only when the condition

$$A = A(\mathrm{Re}, T, P_d) \ge \frac{1}{1 + 2\sqrt{P_d/\mathrm{Re}}} \tag{39}$$

is satisfied [recall that T comes in via λ in (32)]. For a given A between A_b and A_c, the phase plane analysis shows that there are two corresponding values of λ; see Figure 11(b,c). The smaller of these values corresponds to a state in which the channel is constricted ($X < 1$) along its whole length, as represented by the part of the trajectory CDE in Figure 11(b). The larger value of λ, on the other hand, corresponds to a state in which the channel is at first dilated ($X > 1$, trajectory ABC) and then constricted over the downstream portion alone. For this bulged-out case expression (32) for λ

must be modified by the addition of $2\int_1^{h_{max}}[g_1(A)-g_1(h)]^{-1/2}\,dh$, where h_{max} is the maximum channel width. The absence of energy loss in the upstream dilated portion is probably unrealistic, but Figure 11(c) indicates that, for given P_d and Re, a solution to the problem exists for all λ and hence (given the tube length, L) for all T [cf. Jensen & Pedley (1989)].

The bulging value λ_b of λ, demarcating cases constricted everywhere from partially dilated cases, occurs at $A = A_b$ [Figure 11(c)]. Its existence implies that, for given P_d and Re, there is a value of T, equal to T_b, such that $A = A_b$, below which no non-bulging solution exists. If T and P_d were fixed, there would be a bulging value of Re, Re_b say, as shown in Figure 9(a,b). Moreover, we can tell that for given T and Re there is also a bulging value of P_d to keep condition (39) satisfied. Further, for a fixed tension, P_d and Re, there is a bulging value for membrane length (since $\lambda = LT^{-1/2}$).

The curves of λ versus A are shown in Figure 12(a) (for Re = 1, 100, 500), where the corresponding numerical results are also plotted as dashed curves. The circles

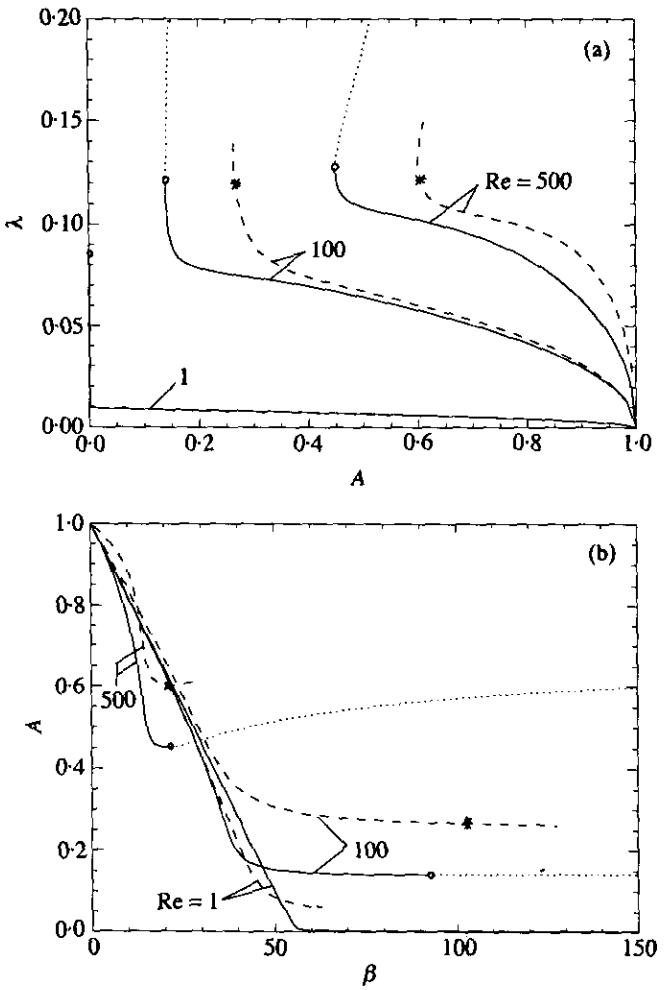

Figure 12. (a) $\lambda(A)$ versus A for Re = 1, 100 and 500. The solid curves are analytical predictions, and the dotted curves are those when the upstream membrane bulges out at $A_b < A < A_c$, with first bulging points marked by circles; the dashed curves are the numerical results, where the first bulging points are marked by stars. For Re = 1, the numerical solution broke down before the bulging point was reached. (b) A versus β for the same parameters.

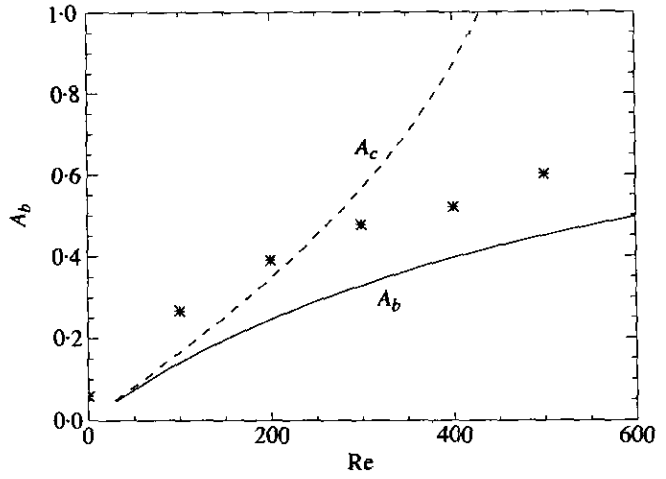

Figure 13. Relationship of the bulging A_b with Re at $P_d^* = P_{d0}^*$, where the solid curve is the analytical model, and stars represent the bulging values obtained from our numerical results. A_c is also plotted as a dashed curve, which increases with Re.

mark the analytical bulging points, when $A = A_b$, while the numerical bulging points are marked by stars. The curves of A versus β for the same parameters are given in Figure 12(b).

More information on the bulging point is given in Figure 13, where A_b obtained from the 1-D model at $P_d^* = P_{d0}^*$ is plotted against Re in the range 1–600, and compared with corresponding plots from the full numerical solution. The limiting area for $\lambda \to \infty$, A_c, is plotted as a dashed curve, which is very close to A_b when Re is small, and moves away from A_b as Re increases. The corresponding curve of T_b^* versus Re is shown in Figure 14. It is of interest to note that there seems to be very good agreement, for Re above about 100, between the values of T_b^* (or equivalently λ_b) obtained from the 1-D model and those from the full numerical solution, and qualitatively good agreement on the values of A_b. It is also noted that the numerical value of A_b is normally higher than

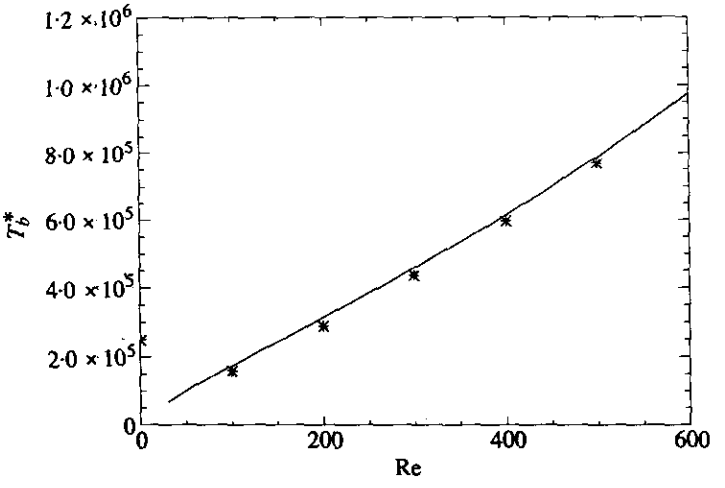

Figure 14. Relationship of the bulging tension, T_b^*, with Re at $P_d^* = P_{d0}^*$, where the solid curve is the analytical prediction, and stars are numerical results.

the results of the 1-D model, while the numerical value of T_b^* is slightly lower than the analytical one. The results in Figure 13 show that the simple model gives a quite good representation of several aspects of the real flow for $\mathrm{Re} \geq 100$ and for $T^* \geq T_b^*$.

6. DISCUSSION

The fact that the breakdown of the numerical solution occurs at a value of T^* only a little above T_b^* suggests that the breakdown is associated with bulging of the membrane at its upstream end and the singularities that develop there. The numerical solution certainly becomes very sensitive to small changes as the bulge point is approached or just passed. However, the non-bulged breakdown of Lowe & Pedley (1994, 1995), and some even more recent computations by Rast (1994), indicate that it would be premature to conclude that the numerical breakdown is definitely due to the presence of a convex corner. There may be other factors which contribute to the numerical breakdown. We have noticed in our computation that convergence becomes extremely difficult to achieve as tension is reduced, even before the wall bulges out: more than 100 iterations become necessary as the tension falls. There are cases when the maximum number of iterations of 200 was reached without convergence (see Figures 7 and 10), before the pressure singularity appeared. This suggests that the numerical system has already become ill-conditioned for small tension. Incorporation of bending stiffness in the elastic segment may assist convergence, and variation of tension due to the shear stress should also be included, as in Lowe & Pedley (1994).

It would be of interest to compare our results with experimental data. The only relevant experiments, however, have been performed with tubes, not 2-D channels. There have been a number of tube experiments in which the downstream transmural pressures and the tension were fixed, while the flow rate was varied [e.g. Bonis & Ribreau (1978), Bertram (1986)]. One interesting common finding was that when the pressure drop increases with flow rate at a given downstream pressure, there seemed to be a point close to $\bar{p}_u = \bar{p}_e$ where steady flow broke down and self-excited oscillations arose.

We will use the 1-D model for the comparison, since it would be very difficult to perform the 2-D simulation either because the Reynolds number was much higher in the experiments (Bertram 1986), or because the tubes were much longer (Bonis & Ribreau 1978). We use the parameters of Bonis & Ribreau (1978): $\bar{L} = 50\,\mathrm{mm}$, $\bar{D} = 1{\cdot}2\,\mathrm{mm}$, $\bar{Q} = 0\text{–}30\,\mathrm{cm^2/s}$, and $\bar{P}_d = 5\text{–}30\,\mathrm{cm\,H_2O}$. The dimensionless parameters become $P_{d0}^* = 7{\cdot}2 \times 10^7 - 4{\cdot}32 \times 10^8$, and $\mathrm{Re} = 0\text{–}3180$. Tension was not mentioned in their paper, but Jensen & Pedley (1989), assuming a longitudinal strain of 12%, estimated the longitudinal tension to be $44{\cdot}32\,\mathrm{N/m^2}$ for the tube. However, it is noted that there is no straightforward way to link the longitudinal tension in a tube with the membrane tension in our 2-D channel. In fact, we found that this estimated tension is much lower than the bulging value when the other parameter values are used in our model (note no upstream bulge was reported in the experiments there, so we assume the bulging value is the limit for the tension); a much larger tension was therefore used instead. This, however, does not affect the results qualitatively.

Figure 15(a) shows the measured results of Bonis & Ribreau (1978) and Figure 15(b) gives the analytical curves of $\Delta\bar{p} \sim \bar{Q}$, using their parameters. The tension was estimated to be $\bar{T} = 20 \times 44{\cdot}32\,\mathrm{N/m^2}$ ($= 886{\cdot}4\,\mathrm{N/m^2}$), or $T^* = 1{\cdot}063 \times 10^{10}$ (therefore, $\lambda = 4{\cdot}05 \times 10^{-4}$). The theoretical curves are terminated where $\bar{Q}$ (or Re) reaches its critical value for upstream bulging (long dashed curve); this value decreases as $\bar{p}_e - \bar{p}_d$ increases. Larger (or smaller) tension only moves the curve further right (or left), but

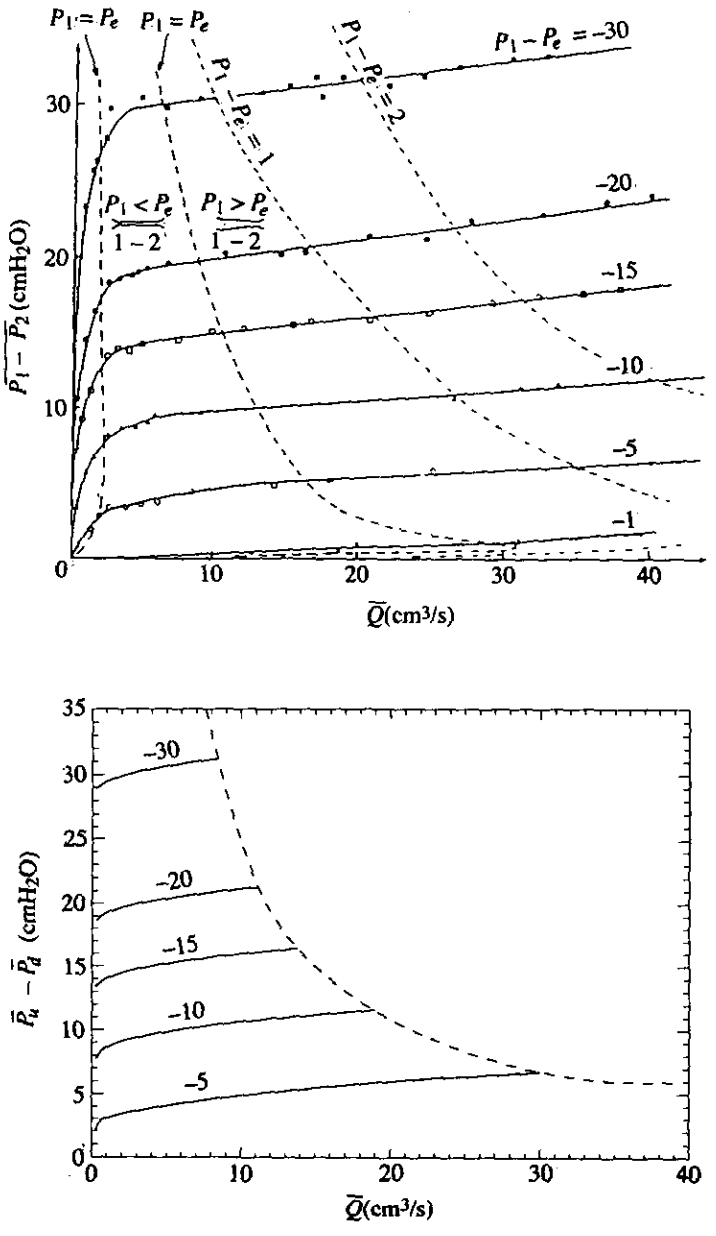

Figure 15. Curves of pressure drop versus flow rate at fixed values of $\bar{p}_e - \bar{p}_d$ measured by Bonis & Ribreau (1978) (reproduced with permission); units of $p_1 - p_e$ are cm H_2O. (b) The same quantities calculated from our 1-D model using their parameter values: $\bar{L} = 0{\cdot}5$ m, $\bar{D} = 1{\cdot}2 \times 10^{-4}$ m, $\bar{U}_0 = 8{\cdot}34 \times 10^{-5}$ m/s, $\bar{P}_d - \bar{P}_e = -5$, -10, -15, -20, -30 cm H_2O, and estimated $\bar{T} = 886{\cdot}4$ N/m. The dashed curve is the bulging value of $\Delta\bar{p}$ when $\bar{Q}$ reaches $\bar{Q}_b$ (or Re reaches Re_b).

will not change the fact that there is a critical curve, and this curve is roughly in the same place at which the experimental steady flow gave way to self-excited oscillations.

What the above comparison demonstrates, then, is that the values of flow rate and downstream transmural pressure at which oscillations are observed in the experiments coincide reasonably well with the values at which the one-dimensional model predicts an upstream bulge, and hence also with values at which the numerical solution breaks

down. This is suggestive, but can be no more than that, for several reasons. First, it is always dangerous to infer any sort of physical breakdown from failure of a numerical scheme to converge; the numerical methods may merely be inadequate. Second, the existence of a steady solution to the governing equations does not mean that it is stable and would be observed in practice; instability analysis or time-dependent computations are essential. Third, there is a considerable discrepancy between our membrane model and the usual description of collapsible-tube elastic properties using a tube law. There is widespread agreement that breakdown of steady flow in many collapsible tube experiments is related to the occurrence of choking, in which the fluid speed somewhere becomes equal to the speed of propagation of long, small-amplitude elastic waves along the tube. In a one-dimensional model in which the elastic wall is an infinite membrane, however, the wave speed tends to the mean fluid speed as the wavelength tends to infinity, so some form of choking seems inevitable [but see Jensen (1990) for a more careful analysis of small oscillations in the finite-length one-dimensional model with longitudinal tension]. Before the mechanism for self-excited oscillations can be properly understood, it is clearly necessary for the present, steady, two-dimensional computation to give way to unsteady computations (which are currently being performed) and, thereafter, to a fully three-dimensional case.

ACKNOWLEDGEMENT

Dr X. Y. Luo is a visiting research fellow at the University of Leeds, on leave from Xi'an Jiaotong University, Xi'an, China. Support provided by the University of Leeds Academic Development Fund is gratefully acknowledged. We would also like to thank Drs N. A. Hill, T. W. Lowe and M. P. Rast for many helpful conversations.

REFERENCES

BERTRAM, C. D. 1982 Two modes of instability in a thick-walled collapsible tube conveying a flow. *Journal of Biomechanics* **15,** 223–224.

BERTRAM, C. D. 1986 Unstable equilibrium behaviour in collapsible tubes. *Journal of Biomechanics* **19,** 61–69.

BERTRAM, C. D., RAYMOND, C. J. & PEDLEY, T. J. 1990 Mapping of instabilities for flow through collapsed tubes of different length. *Journal of Fluids and Structures* **4,** 125–154.

BERTRAM, C. D., RAYMOND, C. J. & PEDLEY, T. J. 1991 Application of nonlinear dynamics concepts to the analysis of self-excited oscillations of a collapsible tube conveying a fluid. *Journal of Fluids and Structures* **5,** 391–426.

BONIS, M. & RIBREAU, C. 1978 Etude de quelques proprietés de l'écoulement dans une conduite collabable. *La Houille Blanche* **3/4,** 165–173.

BRAMLEY, J. S. & DENNIS, S. C. R. 1984 The numerical solution of a two-dimensional flow in a branching channel. *Computers & Fluids* **12,** 339–355.

BROWER, R. W. & SCHOLTEN, C. 1975 Experimental evidence on the mechanism for the instability of flow in collapsible vessels. *ASME Journal of Biomechanical Engineering* **13,** 389–845.

CANCELLI, C. & PEDLEY, T. J. 1985 A separated-flow model for collapsible-tube oscillations. *Journal of Fluid Mechanics* **157,** 375–404.

CONRAD, W. A. 1969 Pressure-flow relationships in collapsible tubes. *IEEE Transactions in Biomedical Engineering* **BME-16,** 284–295.

FIDAP 1992a *FIDAP Theoretical Manual,* 2nd edition. Fluid Dynamics International, Inc.

FIDAP 1992b *FIDAP Users Manual,* 2nd edition. Fluid Dynamics International, Inc.

INGHAM, D. B., TANG, T. & MORTON, B. R. 1990 Steady two-dimensional flow through a row of normal flat plates. *Journal of Fluid Mechanics* **210,** 281–302.

JENSEN, O. E. 1990 Instabilities of flow in a collapsed tube. *Journal of Fluid Mechanics* **220,** 623–659.

JENSEN, O. E. & PEDLEY, T. J. 1989 The existence of steady flow in a collapsed tube. *Journal of Fluid Mechanics* **206,** 339–374.

KAMM, R. D. & PEDLEY, T. J. 1989 Flow in collapsible tubes: A brief review. *ASME Journal of Biomechanical Engineering* **111,** 177–179.

KATZ, A. I., CHEN, Y. & MORENO, A. H. 1969 Flow through a collapsible tube. *Biophysical Journal* **9,** 1261–1279.

LOWE, T. W. & PEDLEY, T. J. 1994 Finite element solution of Stokes flow in a channel with a collapsible segment. In *Computational Methods for Fluid–Structure Interaction* (eds J. M. CROLET & R. OHAYON), pp. 220–229: Harlow, U.K. Longmans.

LOWE, T. W. & PEDLEY, T. J. 1995 Finite element solution of Stokes flow in a channel with a collapsible segment. *Journal of Fluids and Structures* (submitted).

MOFFATT, H. K. 1964 Viscous and resistive eddies near a sharp corner. *Journal of Fluid Mechanics* **18,** 1–18.

PEDLEY, T. J. 1992 Longitudinal tension variation in collapsible channels: a new mechanism for the breakdown of steady flow. *ASME Journal of Biomechanical Engineering* **114,** 60–67.

RALPH, M. E. & PEDLEY, T. J. 1988 Flow in a channel with a moving indentation. *Journal of Fluid Mechanics* **190,** 87–112.

RAST, M. P. 1994 Simultaneous solution of the Navier–Stokes and elastic membrane equations by a finite-element method. *International Journal for Numerical Methods in Fluids* **19,** 1115–1135.

SHAPIRO, A. H. 1977 Steady flow in collapsible tubes. *ASME Journal of Biomechanical Engineering* **99,** 126–147.

SILLIMAN, W. J. & SCRIVEN, L. E. 1980 Separating flow near a static contact line: slip at a wall and shape of a free surface. *Journal of Computational Physics* **34,** 287–313.

TUTTY, O. R. & PEDLEY, T. J. 1993 Oscillatory flow in a stepped channel. *Journal of Fluid Mechanics* **247,** 179–204.

ZIENKIEWICZ, O. C. 1977 *The Finite Element Method,* 3rd edition. London: McGraw-Hill.